

PAPER • OPEN ACCESS

RF antenna helicity dependent particle heating in a helicon source

To cite this article: K J Stevenson *et al* 2024 *Plasma Sources Sci. Technol.* **33** 045009

View the [article online](#) for updates and enhancements.

You may also like

- [Enhanced neutral depletion in a static helium helicon discharge](#)
Saeid Houshmandyar and Earl E Scime
- [Helicon discharges and sources: a review](#)
Francis F Chen
- [Parametric scaling of neutral and ion excited state densities in an argon helicon source](#)
D McCarren and E Scime



Analysis Solutions for your Plasma Research

- Knowledge
- Experience ■ Expertise

[Click to view our product catalogue](#)

Contact Hiden Analytical for further details:
www.HidenAnalytical.com
info@hiden.co.uk



Surface Science

- ▶ Surface Analysis
- ▶ SIMS



Surface Science

- ▶ 3D depth Profiling
- ▶ Nanometre depth resolution



Plasma Diagnostics



- ▶ Plasma characterisation
- ▶ Customised systems to suit plasma Configuration



Plasma Diagnostics

- ▶ Mass and energy analysis of plasma ions
- ▶ Characterisation of neutrals and radicals

RF antenna helicity dependent particle heating in a helicon source

K J Stevenson^{1,*} , T J Gilbert¹, T N Good², M Paul^{1,3}, P Shi^{1,4}, R Nirwan¹, P Srivastav^{1,5}, T E Steinberger¹ and E E Scime¹ 

¹ Department of Physics & Astronomy, West Virginia University, Morgantown, WV 26506, United States of America

² Department of Physics, Gettysburg College, Gettysburg, PA 1732, United States of America

E-mail: ks0213@mix.wvu.edu

Received 11 August 2023, revised 26 January 2024

Accepted for publication 4 April 2024

Published 12 April 2024



Abstract

Experiments have demonstrated that ion phenomena, such as the lower hybrid resonance, play an important role in helicon source operation. Damping of the slow branch of the bounded whistler wave at the edge of a helicon source (i.e. the Trivelpiece-Gould mode) has been correlated with the creation of energetic electrons, heating of ions at the plasma edge, and anisotropic ion heating. Here we present ion velocity distribution function measurements, electron density and temperature measurements, and magnetic fluctuation measurements on both sides of an $m = |1|$ helical antenna in a helicon source as a function of the driving frequency, magnetic field strength, and magnetic field orientation relative to the antenna helicity. Significant electron and ion heating (up to two times larger) occurs on the side of the antenna consistent with the launch of the $m = +1$ mode. The electron and ion heating occurs within one electron skin depth of the plasma edge, where slow wave damping is expected. The source parameters for enhanced particle heating are also consistent with lower hybrid resonance effects, which can only occur for Trivelpiece-Gould wave excitation.

Keywords: helicon source, particle heating, lower hybrid resonance, directional heating, wave modes, laser-induced fluorescence, diagnostics

1. Introduction

While there has been considerable debate about the roles of fast and slow wave damping in the performance of radio

frequency (RF) plasma sources operated in the whistler frequency range (i.e. between the ion cyclotron frequency and electron cyclotron frequency), a number of experiments have demonstrated resonant enhancements of the generated plasma density, electron temperature, and ion temperature near the lower hybrid frequency (LHF). These resonant features point strongly to damping of slow waves in the plasma edge as a significant contributor to the energy input for these ‘helicon’ sources (the ‘fast’ helicon wave has no resonance at the LHF) [1, 2]. Resonant enhancements in the plasma impedance are consistent with predicted excitation of specific helicon wave radial mode structures [3], but the appearance of energetic electrons in the plasma edge under the RF antenna is specifically consistent with slow wave damping on electrons and appears to be independent of radial or axial boundary conditions [4, 5].

³ Currently at the U.S. Naval Research Laboratory, Washington, DC 20375, United States of America.

⁴ Currently at Princeton Plasma Physics Laboratory, Princeton, NJ 08540, United States of America.

⁵ Currently at the Institute for Plasma Research, Gujarat 382428, India.

* Author to whom any correspondence should be addressed.



Original Content from this work may be used under the terms of the [Creative Commons Attribution 4.0 licence](https://creativecommons.org/licenses/by/4.0/). Any further distribution of this work must maintain attribution to the author(s) and the title of the work, journal citation and DOI.

In the first helicon source studies, Boswell proposed that the density in a helicon source should obey a simple bounded whistler, i.e. helicon, wave dispersion relation

$$n \approx \frac{k_{\parallel}^2 c B}{\pi^2 e f} \quad (1)$$

where n is the density, B is the magnetic field strength, e is the electron charge, c is the speed of light, k_{\parallel} is the parallel wave number, and f is the antenna frequency. Note that the density is predicted to scale inversely with wave frequency at constant magnetic field. Therefore, a variable frequency helicon source should be able to vary the plasma density solely through changes in the antenna frequency. Instead, investigations in variable frequency helicon sources demonstrated resonant enhancements of plasma density at specific combinations of antenna frequency and axial magnetic field strength—consistent with a resonance at the LHF [1]. Additional studies focused on ion heating in the perpendicular direction localized to the plasma edge for conditions for which the antenna frequency matched the LHF at the plasma edge [2]. The aim of this study is to contribute to the body of work seeking to uncover answers to the longstanding question and elusive nature of particle heating in helicon plasmas. In this work, we present the results from experiments in the PHASE Space Mapping (PHASMA) experiment. We report ion and electron temperatures, and electron density as a function of antenna frequency, magnetic field strength, and magnetic field direction in a helicon plasma device. We also present radial profiles of the magnetic field fluctuations and compare them to their theoretical counterparts. In section 2, the theory of the dispersion relation and the antenna-wave coupling details are discussed. The experimental apparatus is reviewed in section 3. In section 4, the observations are presented and discussed.

2. Theory

2.1. Dispersion relation

The cold plasma dispersion relation, including ion motion effects and collisions, for typical helicon source plasma parameters is [6]

$$\rho^4 - (\alpha + \beta)\rho^2 + \alpha\beta - \gamma\delta = 0, \quad (2)$$

where $\rho = k_{\perp}$, $\alpha = \varepsilon_1 - N^2 \varepsilon_2^2 / \varepsilon_1$, $\beta = \varepsilon_3 (1 - N^2 / \varepsilon_1)$, $\gamma = N \varepsilon_2 \varepsilon_3 / \varepsilon_1$, and $\delta = N \varepsilon_2 / \varepsilon_1$. $N = k_{\parallel} c / \omega$, and k_{\perp} is the perpendicular wave number. ε_1 , ε_2 , and ε_3 are the elements of the cold plasma dielectric tensor:

$$\varepsilon_1 = l + \sum_{j=e,i} \frac{\omega_{pj}^2 (1 + i \frac{\nu_j}{\omega})}{\omega_{cj}^2 - \omega^2 (1 + i \frac{\nu_j}{\omega})^2}, \quad (3)$$

$$\varepsilon_2 = \sum_{j=e,i} \frac{\sigma_j \omega_{pj}^2 \frac{\omega_{cj}}{\omega}}{\omega_{cj}^2 - \omega^2 (1 + i \frac{\nu_j}{\omega})^2}, \quad (4)$$

$$\varepsilon_3 = 1 - \sum_{j=e,i} \frac{\omega_{pj}^2}{\omega^2 (1 + i \frac{\nu_j}{\omega})^2}, \quad (5)$$

where l denotes the longitudinal mode number, j is the j th species, ω_{cj} is the cyclotron frequency, ω_{pj} is the plasma frequency, ν_j is the total collision frequency, and σ_j is the sign of the charge.

For weak magnetic fields, there is only one solution to the dispersion relation. As the magnetic field strength increases, the single solution bifurcates into two solutions, one with a faster phase speed (the fast wave) than the other (the slow wave). The fast wave solution is the classic helicon dispersion relation for which the perpendicular wave number decreases asymptotically to zero for large magnetic fields and equation (1) is obtained. The perpendicular wavenumber for the slow wave is complex in low density plasmas, thus the wave is strongly damped at the edge of a typical cylindrical plasma source.

Particularly relevant for the work described here, the fast wave perpendicular wave number varies smoothly near the LHF. However, near the lower hybrid resonance,

$$\frac{1}{\omega_{LH}^2} = \frac{1}{(\omega_{ce}\omega_{ci})} + \frac{1}{(\omega_{pi}^2 + \omega_{ci}^2)}, \quad (6)$$

the perpendicular wave number of the slow wave goes to infinity for a collisionless plasma. The collision term, which includes ion-ion, electron-electron, ion-neutral and electron-neutral collisions, reduces the perpendicular wave number of the slow wave at the lower hybrid resonance to a finite value and, for large collision frequencies, slightly shifts the resonant frequency. The corresponding perpendicular phase speed, ω/k_{\perp} , of the slow wave goes to zero. If the wave phase speed becomes comparable to the ion thermal speed, $k_{\perp} v_{thi} / \omega \sim 1$, ion Landau damping is possible [7]. Consistent with the hypothesis of Landau damping of the slow wave on ions, Kline *et al* demonstrated that enhanced perpendicular ion heating in a helicon source occurred for combinations of antenna frequency and magnetic field strength for which equation (6) was satisfied in the plasma edge [2] and for which large-amplitude, very short perpendicular wavelength fluctuations appeared in the plasma edge [8]. Note that in a high-density plasma, the plasma frequency term (the second term on the RHS) in equation (6) vanishes and therefore the LHF is typically considered to be the geometric mean of the ion and electron cyclotron frequencies. However, in a low density plasma, such as at the edge of a helicon source, the plasma frequency term must be included and the net effect is a downshift of the lower hybrid resonance to a lower frequency. It was at the downshifted lower hybrid resonance that the enhanced ion heating was observed in the Kline *et al* work.

More recently, Aguirre *et al* demonstrated that at the conditions of the lower hybrid resonance in low pressure helicon plasmas (very large collisional mean free paths), an annulus of energetic electrons is created underneath the RF antenna [4, 9]. Other groups have since reported similar observations

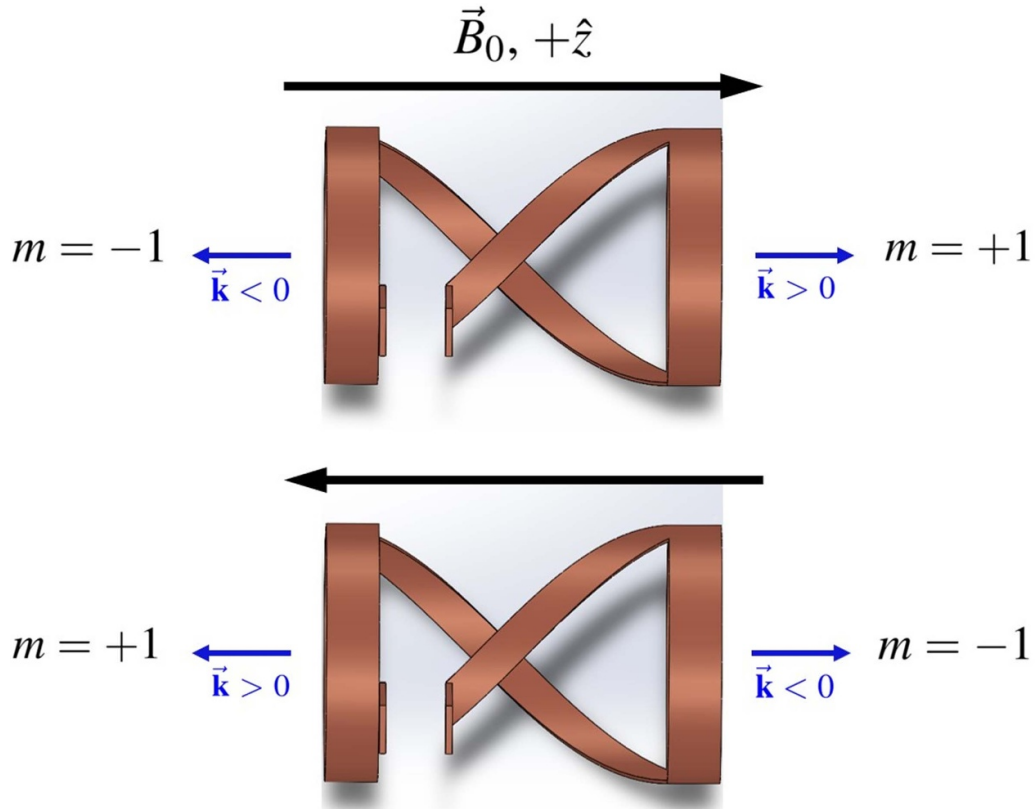


Figure 1. The modes excited by a half-wavelength helical antenna. The top figure depicts a rightward facing background magnetic field, and the bottom figure depicts the modes when the field is reversed. Note that when \vec{B}_0 changes sign, $+\hat{z}$ also changes sign and hence the sign of \vec{k} . This figure corresponds to the naming convention for the PHASMA device (discussed later).

of energetic electron production at the plasma edge, providing further evidence of substantial wave damping in the plasma edge [5]. Such damping could be responsible for the highly efficient coupling of RF power into helicon sources when they are operated near the LHF.

2.2. Antenna coupling

One of the unique features of the PHASMA device is that there is access to the plasma on both sides of the helicon antenna. Typically, antennas are located at one end of a helicon source and thereby diagnostic access is limited to only one side of the antenna. A 19 cm $m = |1|$ half-wavelength helical antenna located 125 cm from the smaller radius end of the chamber is used to produce the plasma. Helical antennae emit waves to either side of the antenna. If we define $z=0$ at the geometric center of an arbitrary antenna, a wave with wavevector $\vec{k} > 0$ is launched to the $z > 0$ side of the antenna and a wave with $\vec{k} < 0$ is launched to the $z < 0$ side of the antenna (see figure 1). Note that figure 1 is a simplified picture of the wave propagation. In reality, the waves do not always propagate exactly along \vec{B}_0 , but instead propagate within the resonance cone defined by the angle $\theta = \arccos(\omega/\omega_{ce})$ [10, 11]. The $m = +1$ and $m = -1$ modes are the right-hand circularly polarized (RHCP) and left-hand circularly polarized (LHCP)

modes, respectively, referring to the azimuthal mode number in the wave equation solutions, $\vec{E}, \vec{B} \sim \exp[i(m\theta + kz - \omega t)]$. Half helical antennae have a unique feature in that they are directional, in relation to the background magnetic field, \vec{B}_0 . That is, an $m = +1$ helical antenna subject to a background magnetic field pointing in the $+\hat{z}$ direction becomes an $m = -1$ helical antenna if the direction of \vec{B}_0 is reversed. Thus, investigation of both antenna helicities is possible for the same system parameters by changing the direction of \vec{B}_0 . Note that the convention in plasma physics is to define the wave polarization with respect to the static background magnetic field \vec{B}_0 (as opposed to \vec{k} as in other fields of physics). Therefore, the $+\hat{z}$ direction is always defined as the direction of $+\vec{B}_0$. It follows that when \vec{B}_0 is reversed in the lab frame, the direction of $+\hat{z}$ and $+\theta$ in the solutions of the wave equation also reverse.

The electrostatic field of the antenna arises from the space charge distribution created by the fields induced by the RF currents in the antenna. It is believed that the electrostatic electric field is how the RF wave couples to the wave field in the plasma. Previous experiments [12–15] reported more efficient coupling of power into the plasma (higher plasma densities) when the antenna helicity and magnetic field direction were chosen to launch $m = +1$ mode waves into the vacuum chamber. Based on theoretical predictions for the different wave helicities, Light and Chen *et al* argued that the

narrower field profile (more restricted radial extent) of the $m = -1$ mode prevents it from coupling as effectively to the waves in the plasma [12]. A more recent study demonstrated that the efficient coupling of the $m = +1$ mode is caused by peaked radial density profiles (i.e. a radially inward density gradient) which attenuate left-hand helicon modes and enhance right-hand modes [16].

3. Experimental apparatus

3.1. PHASMA

PHASMA is designed to study space plasma-relevant phenomena, including particle heating and acceleration at kinetic scales during magnetic reconnection, [17, 18] electromagnetic instabilities driven by ion temperature anisotropy and plasma pressure [19], ion acceleration in expanding plasmas [20], and cross-field ion flows near plasma-material interfaces immersed in a magnetized, high-density plasma [21]. A key feature of PHASMA is the availability of volumetric, non-perturbative, laser diagnostics for ion and electron velocity distribution function measurements with spatial resolution at the kinetic, gyroradius, scale (\sim mm for electrons) on both sides of the RF antenna. State-of-the-art laser induced fluorescence (LIF) schemes are available to measure velocity distribution functions of ions [8, 22] and neutrals. [23–25] An incoherent Thomson scattering system [26, 27] provides measurements of the electron velocity distribution function.

As shown in figure 2, PHASMA consists of two sections, a helicon plasma source in a vacuum chamber 1.7 m in length and 15 cm in diameter and another vacuum vessel 2.7 m in length and 40 cm in diameter (henceforth referred to as the upstream and downstream regions, respectively). The 19 cm half-wavelength helical antenna is located at $z = 125$ cm from the helicon source end of the facility (see figure 3), thereby enabling measurements of plasma production and heating on both sides of the RF antenna. The three turbomolecular pumps located at the ends of the system provide a total pumping speed of 38001 s^{-1} and maintain a base pressure of $< 2 \times 10^{-7}$ Torr. A static axial magnetic field of up to 2000 Gauss in the upstream region (375 Gauss in the downstream region) is generated with 22 electromagnet coils. Various magnetic field configurations, uniform, flared, and magnetic mirror are created by varying the relative currents in the coils. The helicon source operates at antenna frequencies of 9–15 MHz and RF powers up to 1.5 kW to create steady-state and pulsed plasmas in argon, helium, and xenon [2, 8, 28]. PHASMA accesses a wide range of magnetized plasma operational regimes, e.g. plasma beta $nk_B T / (B^2 / 2\mu_0) \approx 0.001 \sim 1$ and Lundquist number $\mu_0 L V_A / \eta \approx 1 \sim 100$, by independently controlling the plasma density and magnetic field strength.

Argon gas is injected on the upstream side of the vacuum chamber and the mass flow rate of the gas was maintained at 50 SCCM for all the experiments reported here. The resultant operating pressure in the upstream chamber was ~ 3.3 mTorr as measured at the upstream turbo pump and ~ 0.4 mTorr as

measured at the two downstream turbo pumps at the end of the PHASMA chamber.

RF power was provided by an E&I A-1000 amplifier driven with a Stanford Research Systems DS345 function generator. Forward and reverse power was measured at the output of the amplifier. Reflected power was manually minimized using a capacitive matching network in a balanced π configuration [1]. The matching network is balanced in the sense that neither side of the antenna is tied to ground through the matching network. Instead, the antenna potential is allowed to float relative to the chamber and electrical ground of the matching network is established at the junction of the tuning and load capacitors. The parameters varied in this work were the background magnetic field and antenna frequency; the upstream field was discretely varied from ~ 530 G to ~ 1840 G and the antenna frequency was discretely varied from 9–13 MHz. The downstream field was not varied directly, rather, its magnitude changed as the upstream field was varied. These measurements were repeated for both background magnetic field directions (east and west in the lab frame). Table 1 lists the parameters that were held constant throughout all measurements.

3.2. Diagnostics

3.2.1. LIF. A rendering of the device (depicted without magnetic coils) outlining the diagnostic locations is given in figure 3. Details of the measurement locations are provided in table 2. The diagnostics used in these experiments are LIF, RF compensated Langmuir probes, and magnetic fluctuation sense coils placed in the upstream and downstream regions. LIF provides non-perturbative measurements of the ion velocity distribution function (IVDF) in the plasma. A laser is swept through an absorption transition of the target ion species while recording emission from the excited upper state of the transition. The absorption line is broadened by the Doppler shifts of the thermally distributed ion velocities. The measured absorption lineshape is converted into velocity space by

$$V = \frac{f - f_o}{f_o} c, \quad (7)$$

where f is the laser frequency in the lab frame, f_o is the frequency of the transition for the ion at rest, V is the velocity of the ion, and c is the speed of light in vacuum.

The Ar II transition used for these experiments begins with the $3d'2G_{9/2}$ collisionally excited metastable state. This state is produced from ground state neutral atoms, ions in other electronic states [29], or step-wise excitation [30]. The metastable density is related to the LIF signal, which previous experiments have shown is roughly proportional to the square root of the product of ion density, electron density, and temperature: $I_{\text{LIF}} \propto \sqrt{n_i n_e T_e}$ [31]. The metastable state is pumped to the $4p'2F^0_{7/2}$ state at a vacuum wavelength of $\lambda = 611.662$ nm. The upper state then decays to the $4s'2D_{5/2}$ state with the emission of a photon at 461.086 nm [32]. For perpendicular IVDF measurements, the laser light is injected perpendicular to the chamber axis and the injected light is polarized

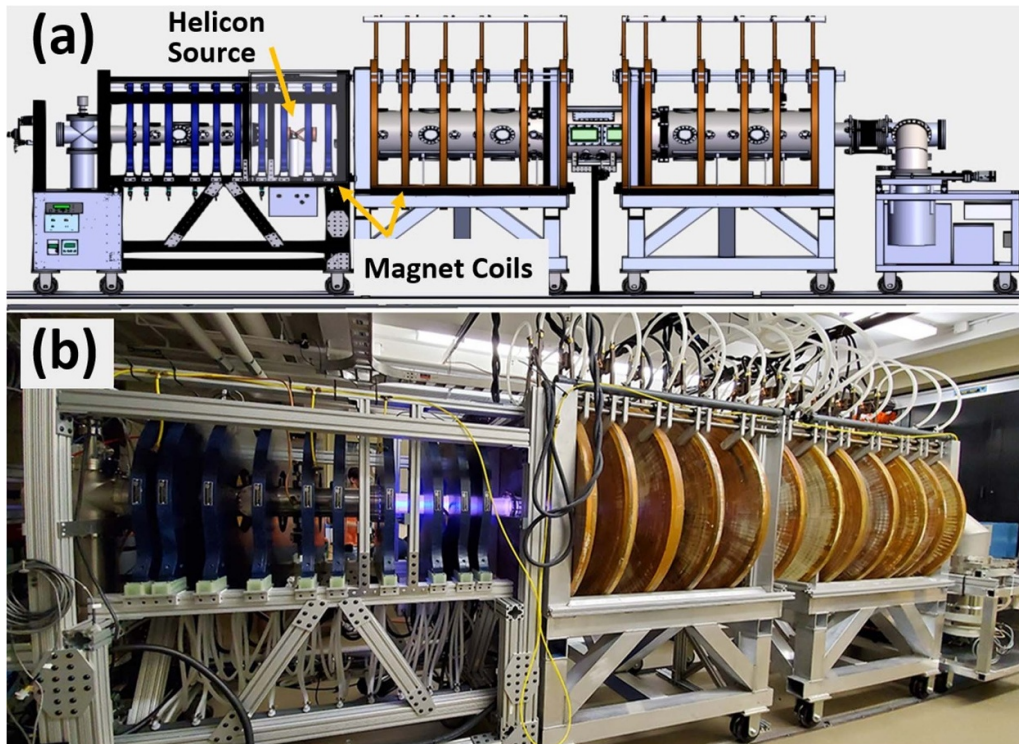


Figure 2. (a) CAD model of the PHASMA facility highlighting the helicon source. Three turbomolecular drag pumps maintain a base pressure of $<2 \times 10^{-7}$ Torr. Twenty-two solenoid coils are used to generate the background axial magnetic field. (b) Photo of PHASMA with helicon plasma source operating.

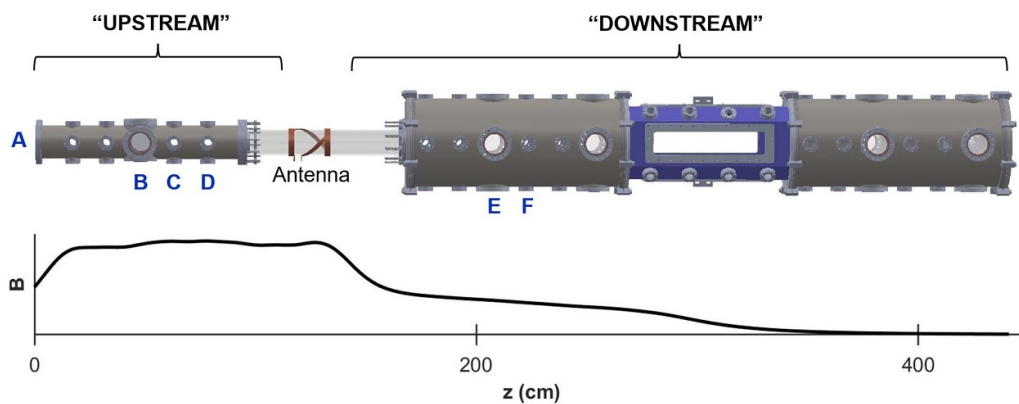


Figure 3. A rendering of the source chamber and the PHASMA device (without magnet coils) showing the locations of the measurements (identified by the capital letters). Port locations for the diagnostics are given in table 2. The length of the device is 4.4 m and the axial magnetic field profile is plotted to scale.

parallel to the background magnetic field so that only the π transitions of the Zeeman split states are excited. For parallel IVDF measurements, the laser is injected along the magnetic field and is circularly polarized so that only one of the circularly polarized σ transitions is excited. Stark, Zeeman, natural, and laser linewidth broadening are negligible for these experimental conditions and are ignored in the analysis [33]. The laser powers delivered to the experiment were consistently below the threshold at which laser broadening appreciably contributed to the measured distribution. Typical perpendicular and parallel IVDFs taken at the center of the plasma are shown in figure 4. By splitting the laser light into two

equal power beams and using two sets of collection optics for perpendicular measurements, upstream and downstream LIF measurements are acquired simultaneously. The same two collection optics provide simultaneous upstream and downstream parallel LIF measurements for a single injection beam.

The wavelength of a Sirah Matisse dye laser is swept up to $\Delta f = \pm 10$ GHz around the transition wavelength of the initial metastable state over a 180 s scan time. 10% of the output of the laser is sampled by a Bristol 621 wavelength meter with an accuracy of ± 0.0002 nm. The absolute wavelength is determined with an iodine reference cell. The beam is mechanically chopped at 5 kHz and coupled into a 200 μm core

Table 1. The fixed parameters for all configurations.

Fixed parameter	Value
RF forward power	760 W (± 10 W)
RF reflected power	$< 10\%$ of P_{forward}
Fill pressure	3.3–3.4 mTorr
Mechanical chopper for LIF	5 kHz
Scan time/time constant ratio for LIF	180

Table 2. Measurement locations on the device and relative to the middle of the antenna.

Measurement	Port	Axial location (cm)	Distance from center of antenna (cm)
\parallel LIF injection	A	0	125
Radial LIF	B	43	82
Upstream LP, radial LP	C	63	52
Upstream magnetic sense coil	C	63	62
Upstream \perp LIF injection	D	73	52
Upstream \perp, \parallel LIF collection	D	73	52
Downstream LP	E	200	75
Downstream magnetic sense coil	F	215	90
Downstream LIF injection/collection	F	215	90

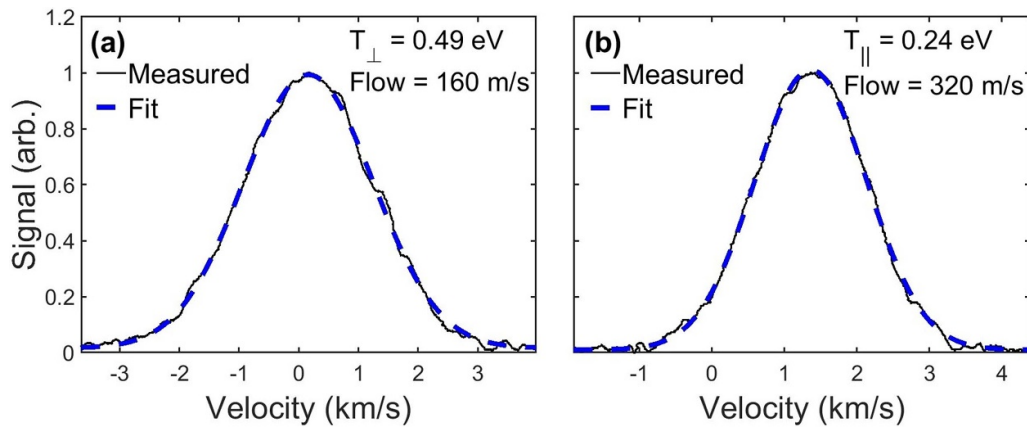


Figure 4. (a) A typical perpendicular IVDF as measured with LIF (LIF signal versus velocity) and a Maxwellian velocity distribution fit. The resultant temperature and flow from the fit are $T_{\perp} = 0.49$ eV and $v_r = 160$ m s $^{-1}$, respectively. (b) A typical parallel IVDF and a Maxwellian velocity distribution fit. The resultant temperature and Zeeman-corrected flow from the fit are $T_{\parallel} = 0.24$ eV and $v_z = 320$ m s $^{-1}$, respectively. Both measurements were obtained upstream at a driving frequency of 9.5 MHz and an eastward background magnetic field of ~ 1200 G.

multimode optical fiber. Light carried through the fiber is then injected into the plasma through a collimator in $-\hat{x}$ and fluorescence is collected in $+\hat{y}$ by optics with a spatial resolution of 1 mm. The collection optics transmit fluorescent light through a 200 μm multimode fiber to a Hamamatsu HC124-06 photomultiplier tube (PMT). Background emission is rejected by a 1 nm bandpass filter centered at 461 nm. LIF signal is distinguished from spontaneous emission by a Stanford Research Systems SR830 lock-in amplifier referenced to the chopper frequency and integrated over 1 s. The optical layout for the LIF measurements is shown in figure 5.

3.2.2. Langmuir probes. To measure the electron density, n_e , and electron temperature, T_e , two (one $\varnothing 0.3$ mm \times 2 mm and one $\varnothing 0.5$ mm \times 5 mm) graphite tip Langmuir probes are inserted into the plasma upstream and downstream of the RF antenna at $z = 63$ cm and $z = 200$ cm, respectively. The probes are RF compensated at the first and second harmonics of the antenna frequency. Simple Langmuir analysis techniques are problematic for magnetized RF plasmas [34, 35]. A probe will collect electrons along the magnetic field lines it intersects in addition to electrons transported across field lines to the probe surface. If the electron gyroradius of the system is close to the probe dimensions, given by $\rho_e \sim r_p \ln l_p / r_p$ where r_p and l_p are

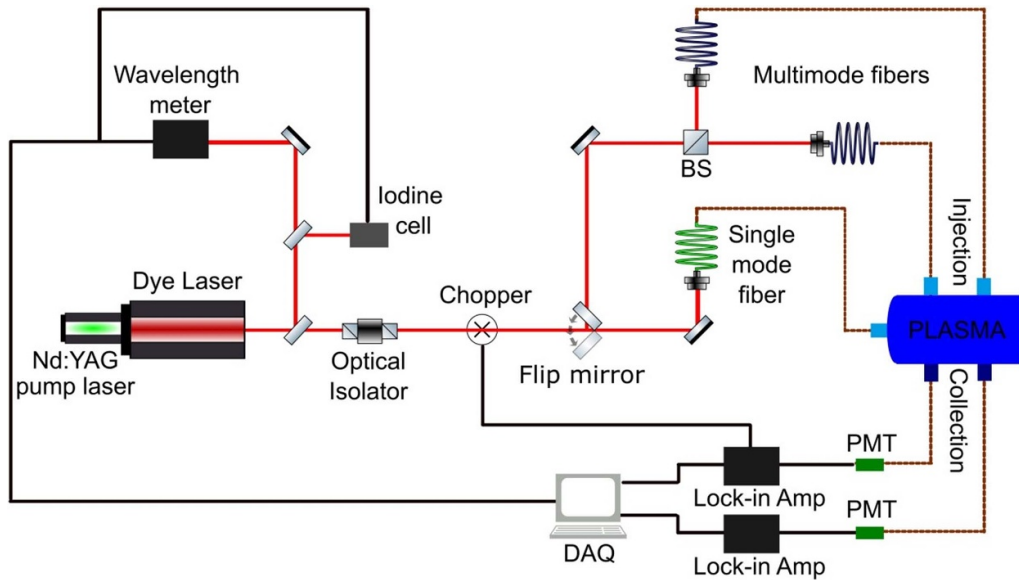


Figure 5. The injection and collection optics along with a schematic of the laser system used for the dual perpendicular and dual parallel measurements.

probe radius and length respectively, then current collection by the probe can be approximated by the Druyvesteyn method as detailed in previous work [21]. The Druyvesteyn method does not assume a particular distribution for the electrons when calculating n_e and T_e . This approach yields an effective electron temperature despite non-Maxwellian features.

3.2.3. Magnetic fluctuation coils. Two magnetic fluctuation sense coils were used to measure the B_z and B_θ components of the radial helicon wave profile in the downstream and upstream regions (locations C and F in figure 3). Each magnetic probe is comprised of a 2.5 mm ID ($\varnothing 3.4$ mm) two-turn coil made of insulated copper wire wrapped around a boron nitride spool with the leads wound into a twisted pair. The sense coil is protected from the harsh environment of the helicon plasma by a fiberglass heat guard which is wrapped in grounded copper foil to block electrostatic fields in the plasma. The entire coil and shielding is encased in a $\varnothing 1/4$ inch ceramic tube. The ceramic tube extends 12 cm from where it is joined to the probe shaft with a reducing union. The twisted pair extends the length of the probe shaft (55 cm) and each end of the pair is connected to a BNC feedthrough and then to a hybrid combiner. Since RF sources are fraught with electromagnetic noise, a hybrid combiner is used to reject any electrostatic noise that couples to the coil through the copper foil. A 9–15 MHz RF filter follows the hybrid combiner to ensure only the first harmonic signal is measured. A LeCroy WaveRunner 6 Zi oscilloscope is used for data acquisition and each measurement is an average of at least 200 individual time series measurements.

4. Experimental measurements

In this article, we employ the naming convention defined in figure 6 which corresponds to the antenna coupling illustrated in figure 1. For example, as depicted in the bottom cartoon of figure 6, measurements taken on the upstream side of the antenna when the background magnetic field is pointing towards the upstream side are labeled ‘upstream⁺’, to correspond to the $m = +1$ side of the antenna defined by the direction of \vec{B}_0 . It follows that measurements taken on the downstream side (when the field is pointed towards the upstream side) are labeled ‘downstream⁻’, since this region corresponds to the $m = -1$ side of the antenna.

4.1. Comparing upstream and downstream measurements

Shown in figure 7 are contour plots of the perpendicular and parallel ion temperature, and electron temperature and density, as a function of the RF driving frequency, magnetic field strength, and magnetic field direction. For these measurements, the background magnetic field was varied from ~ 530 G to ~ 1840 G in 7 increments and the antenna frequency was varied from 9–13 MHz in increments of 0.5 MHz. Therefore, each contour plot is made up of 63 different plasma source configurations. Note that the color bars for most plots are different because of dramatic changes in absolute values. By comparing figures 7(a) and (b), we see that the overall upstream ion temperatures are significantly hotter than the downstream ion temperatures. As expected, the downstream plasma density is less than upstream density due to the expanding magnetic field geometry (from the

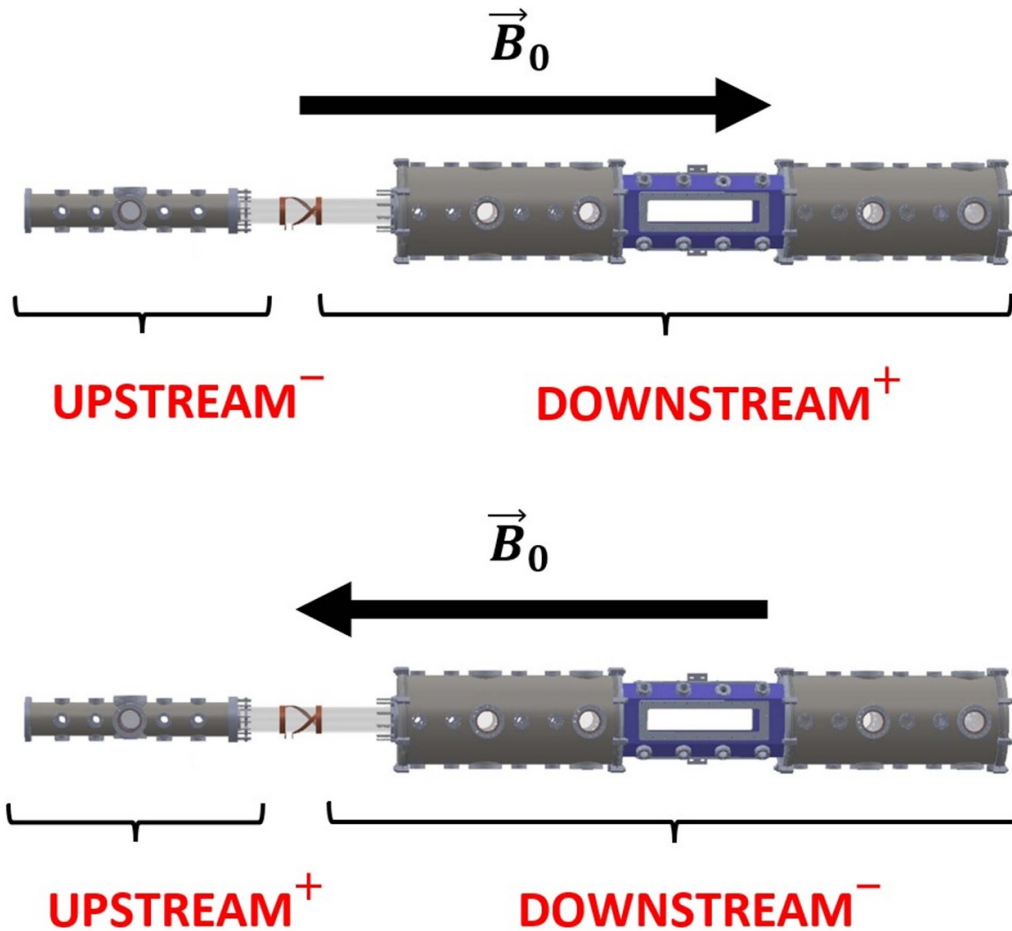


Figure 6. The naming convention for the PHASMA device is such that the ‘Xstream⁺’ corresponds to the the direction that the background magnetic field is pointing towards.

11.7 cm diameter source region to the 40 cm diameter downstream region). Upstream, the ion temperatures are clearly anisotropic (note the different color bars for parallel and perpendicular ion temperatures), with the perpendicular ion temperature nearly double that of the parallel ion temperature. Figure 8 shows that the ion temperature anisotropy is enhanced in the downstream⁻ and upstream⁻ cases (i.e. the $m = -1$ regions). The ion temperature anisotropy in these cases is particularly enhanced because the parallel ion temperatures are so small.

4.2. Comparing upstream⁺ vs. upstream⁻ and downstream⁺ vs. downstream⁻

Comparing the upstream⁺ columns to the upstream⁻ columns shows that the upstream⁺ ion temperatures, electron temperatures, and plasma densities are higher than the upstream⁻ case. In fact, the ion and electron temperatures in the upstream⁺ case are up to two times greater than in the upstream⁻ case. There are clear resonance features in the upstream⁺ cases, characterized by peaks in temperatures and densities at certain magnetic field and driving frequency

combinations. The enhanced ion temperatures and densities are due to the TG resonance at the LHF, which will be discussed in section 4.4, and further in section 5. In the upstream⁺ electron temperature map, there is a band of enhanced temperatures that begins at a magnetic field of 800 G and a driving frequency of 9 MHz that extends through the data to a magnetic field of 1600 G and a driving frequency of 13 MHz. In PHASMA, the electron-ion collision frequency ranges from ≈ 5 –100 MHz (depending on the temperature and density). Resonances in the ion temperature occur near the LHF, from 9–13 MHz in PHASMA. As such, it is not unreasonable to infer that the enhanced electron temperatures are a result of electron-ion collisions between electrons and the LHF resonance heated ions. For large values of electron density, the LHF is linearly proportional to magnetic field strength, the same trend seen in these enhanced electron temperature values. The ion temperatures (both parallel and perpendicular) in the upstream⁺ case divide up into two regions (left side and right side of each plot), one with ion temperatures roughly twice as large as the other. The driving frequency and magnetic field combinations that form the boundary between these regions of different temperature also scale linearly with the LHF (consistent with the scaling of

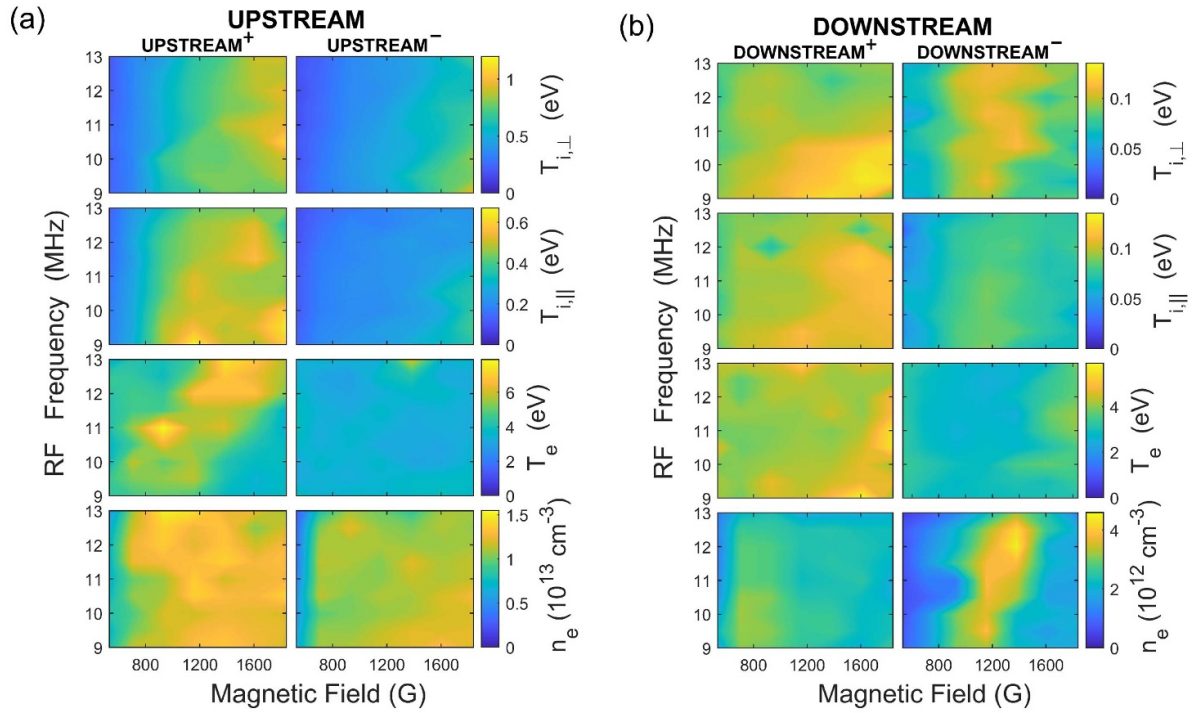


Figure 7. Contour plots of the (a) upstream and (b) downstream ion temperature, electron temperature, and electron density, as a function of the antenna frequency, the magnetic field strength, and the magnetic field direction.

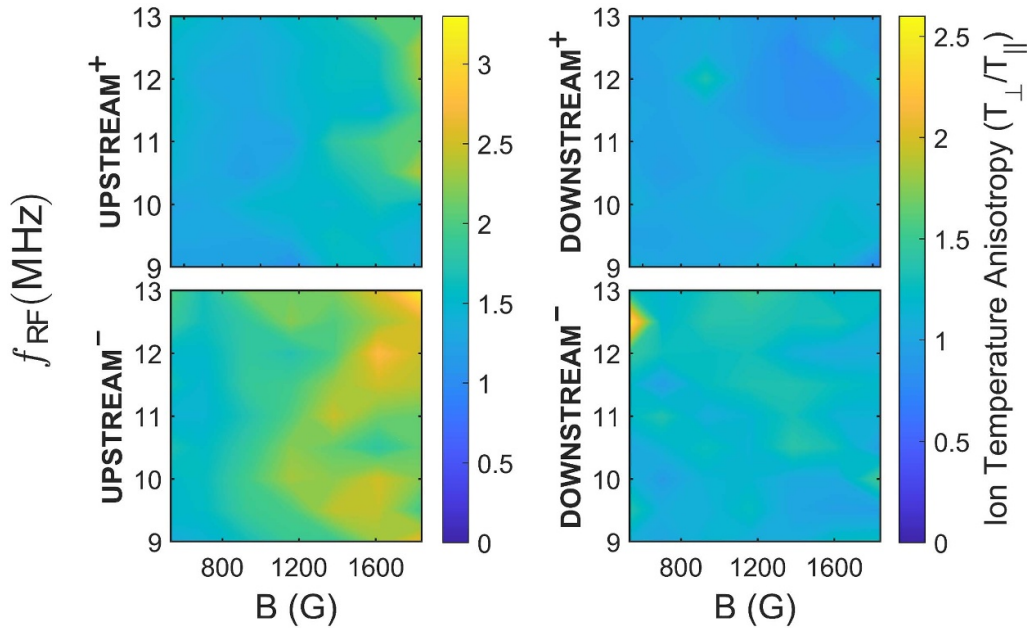


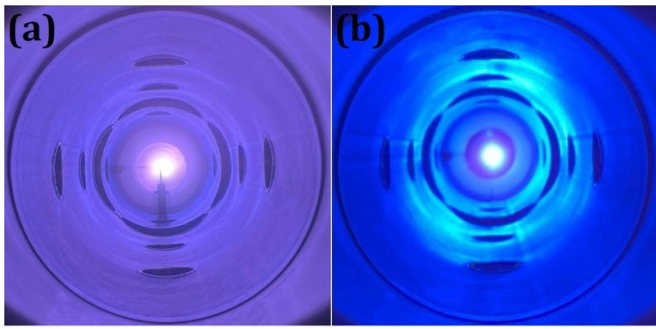
Figure 8. Contour plots showing that ion thermal anisotropy is enhanced for the downstream⁻ and upstream⁻ cases. Ion thermal anisotropy in the upstream⁻ configuration is particularly enhanced because of the very low parallel ion temperatures in that configuration, not because of larger perpendicular ion heating. Note that the color bars for the downstream and upstream plots are different.

the resonance feature in the electron temperature measurements). The average plasma density in the upstream⁺ case is slightly larger than for the upstream⁻ case. So, for the same source RF power and magnetic field strength, simply reversing the magnetic field direction results in particle temperatures up to two times larger at comparable plasma densities.

We see a similar preference for particle heating in the downstream measurements, i.e. the downstream⁺ ion and electron temperatures are larger than for the downstream⁻ case. Note that for the downstream⁺ case, the electron temperatures and parallel ion temperatures are up to two times larger compared to the downstream⁻ case. In contrast to the upstream measurements, the resonance feature in the plasma

Table 3. Summary of the + and – configuration measurements.

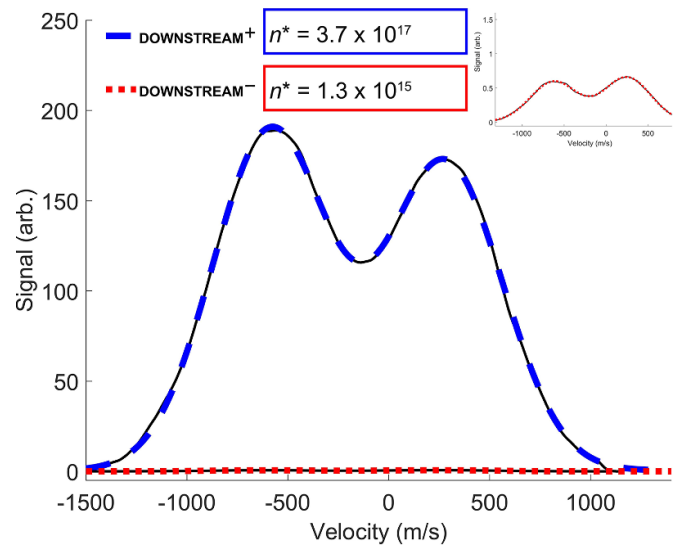
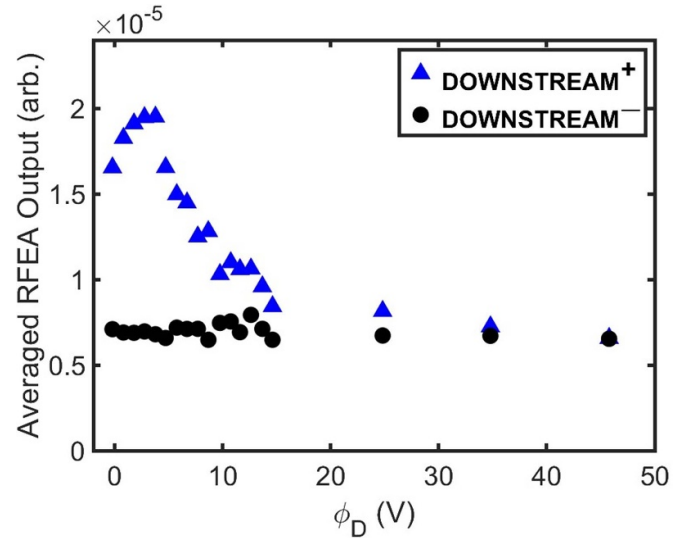
	+ configuration	– configuration
Upstream	larger T_i larger n_e larger T_e edge ion heating edge e^- heating	smaller T_i smaller n_e smaller T_e no edge ion heating edge e^- heating larger T_i anisotropy
Downstream	similar T_i smaller max n_e , larger $n_{e,avg}$ larger T_e	similar T_i larger max n_e , smaller $n_{e,avg}$ smaller T_e larger T_i anisotropy


Figure 9. Photographs taken at an axially mounted window on the upstream end of the PHASMA apparatus for the (a) upstream– and (b) upstream+ magnetic field configurations.

density and perpendicular ion temperatures occurs for the $m = -1$ field orientation (the downstream– case). However, the downstream+ case (averaged over all source parameters) still has a slightly larger average n_e , with $n_{e,avg} = 1.9 \times 10^{12} \text{ cm}^{-3}$ for the downstream+ case and $n_{e,avg} = 1.7 \times 10^{12} \text{ cm}^{-3}$ for the downstream– case. Table 3 summarizes these measurements in terms of the magnetic field direction.

The higher plasma densities and electron temperatures in the upstream+ case correspond to distinct differences in plasma appearance. As shown in figure 9, the upstream+ configuration has a very bright and intense blue core, whereas the plasma in the upstream– configuration is not as bright and has a diffuse violet hue (corresponding to more neutral argon emission instead of blue emission more typical of ion lines). Note that these photos were taken for the same magnetic field strength, fill pressure, and antenna frequency—the only difference being the background magnetic field direction.

Other measurements, consistent with the Langmuir probe measurements shown in figure 7(b), also indicate a decrease in electron energization/heating for the downstream– case. For example, neutral argon LIF measurements (see [36] for a detailed discussion of neutral argon LIF in PHASMA) were performed in the downstream chamber for the downstream+ and downstream– cases. The LIF-measured metastable ion densities differed by two orders of magnitude (see figure 10). Such a dramatic decrease in neutral LIF metastable density


Figure 10. The downstream neutral LIF signals for the downstream– (red dotted) and downstream+ (blue dashed) cases. Note that the LIF signal amplitude differs by two orders of magnitude. The inset shows an enlarged plot of the downstream– LIF signal. The uncalibrated metastable densities, n^* (the integral of the LIF signal) are given for each case. These measurements were obtained at $f_{RF} = 10 \text{ MHz}$ and $B_0 \approx 320 \text{ G}$ in the downstream region (1157 G in the upstream region).

Figure 11. The flux of electrons with energies greater than the discriminator voltage (ϕ_D) as measured with a retarding field energy analyzer.

requires a dramatic reduction in the number of energetic electrons available to excite the neutrals to the necessary metastable state. The near total absence of energetic electrons in the downstream– case was confirmed with downstream retarding field energy analyzer (RFEA) measurements (figure 11). The RFEA measurements of electron fluxes, at all energies, were orders of magnitude smaller for the downstream– case.

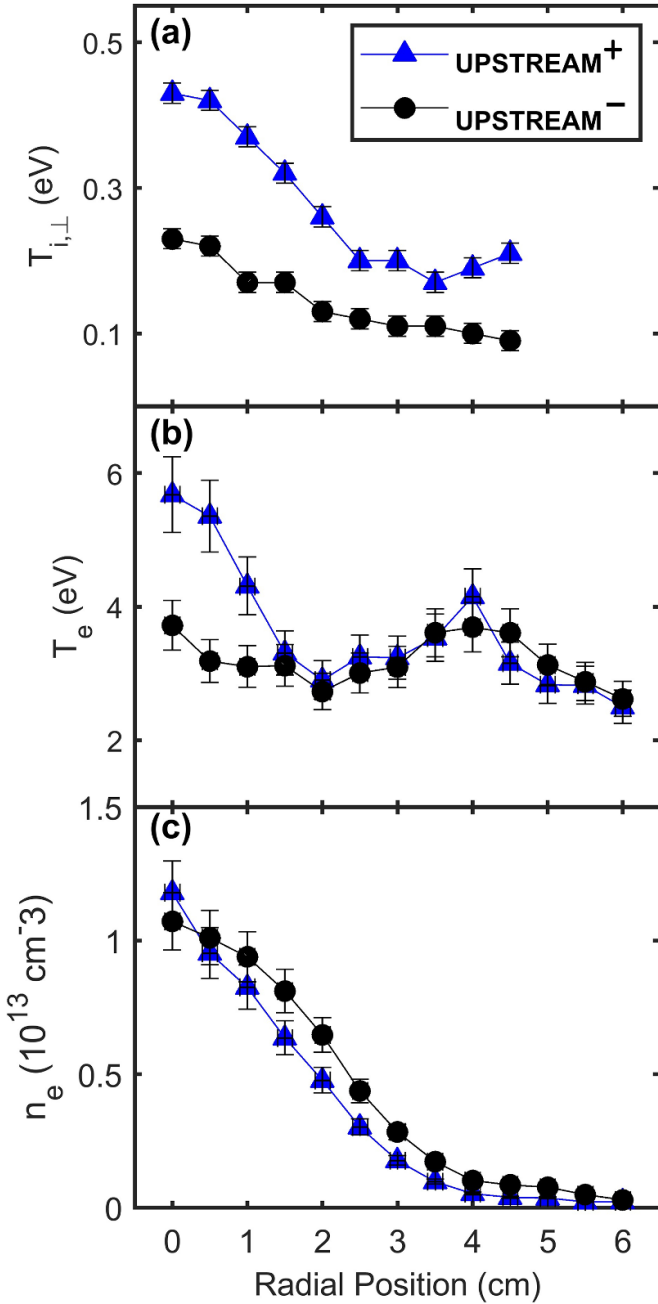


Figure 12. Radial profiles of (a) the perpendicular ion temperature, (b) the electron temperature, and (c) the plasma density. The ion temperatures were measured with LIF at $f_{\text{RF}} = 9.5$ MHz and $B_0 = 930$ G. T_e and n_e were measured with a compensated Langmuir probe at $f_{\text{RF}} = 10$ MHz and $B_0 = 1157$ G.

4.3. Radial temperature and density measurements

Figure 12 shows the upstream radial temperature profiles for both magnetic field orientations. The ion and electron temperatures in the upstream⁺ cases are higher than the corresponding temperatures in the upstream⁻ cases, as expected, considering the measurements discussed in section 4.2. Figure 12(b) shows a spike in the electron temperature around $r = 4$ cm (towards the edge of the plasma) in *both* the upstream

cases, while figure 12(a) shows that the perpendicular ion temperature only peaks for the upstream⁺ case (and not the upstream⁻ case). The reason for the absence of ion edge heating in the upstream⁻ case is not clear. For both electrons and ions, enhanced heating happens around the same location of $r = 4$ – 4.5 cm. The electron skin depth for these plasma conditions ($d_e = c/\omega_{pe} \approx 1.5$ cm, where c is the speed of light and ω_{pe} is the electron plasma frequency). Given that the plasma chamber radius is 5.9 cm under the antenna, the peaks in electron and ion heating occur roughly one electron skin depth into the plasma, exactly where such heating would be expected for a slow wave damped at the plasma edge. These measurements of electron heating in the edge are consistent with the previous measurements of Aguirre *et al* [9]. Furthermore, previous studies [37, 38] have established that the slow wave (i.e. the Trivelpiece-Gould mode) deposits most of its power at the edge of the plasma due to strong damping of the TG wave at the plasma boundary. Therefore, the edge heating observed in these upstream temperature measurements is likely indicative of excitation and damping of the TG mode.

Because there was some concern that a decrease in plasma density at the edge might introduce an artificial increase in the measured perpendicular ion temperature through power saturation effects (power saturation occurs in LIF measurements if the laser power is too large for a given metastable ion density), the ion temperature was measured as a function of laser power (for both magnetic field directions), ensuring that power saturation was not affecting the ion temperature measurement.

4.4. Resonances at the LHF

Previous studies of RF power coupling in helicon sources determined that heating of ions in the perpendicular direction is a unique signature of resonant damping of the slow wave [1], and that such heating is particularly enhanced at the edge of the plasma where slow wave damping is predicted by theory [2, 37]. The measurements shown in figure 7 are plotted again in figure 13 along with the LHF, based on the plasma density at $r = 0$ and 52 cm from the center of antenna, overlaid on the measurements (dotted black line). To calculate the LHF at the plasma edge (dashed white line), the plasma density at the chamber edge, $r \sim 7$ cm, is estimated by extrapolating the measured density profile (figure 12(c)) to $r = 7$ cm using a fit to the measured density profile. The black dotted line marking the LHF in figure 13 is effectively the upper limit of the LHF and has almost no dependence on density (recall that for large densities, the LHF is essentially the geometric mean of the ion and electron cyclotron frequencies). As the density decreases, the LHF becomes more sensitive to density and shifts to lower frequencies for the same magnetic field strength, i.e. towards the white dashed line that represents the LHF at the edge. To be clear, the density near the antenna is the preferred density value to use in calculating the LHF since studies have shown that most power deposition occurs close to the antenna [39, 40]. However, due to limited probe access near the antenna, the closest density measurement was 52 cm from the center of the antenna. Previous helicon discharge studies [3, 14, 39, 41]

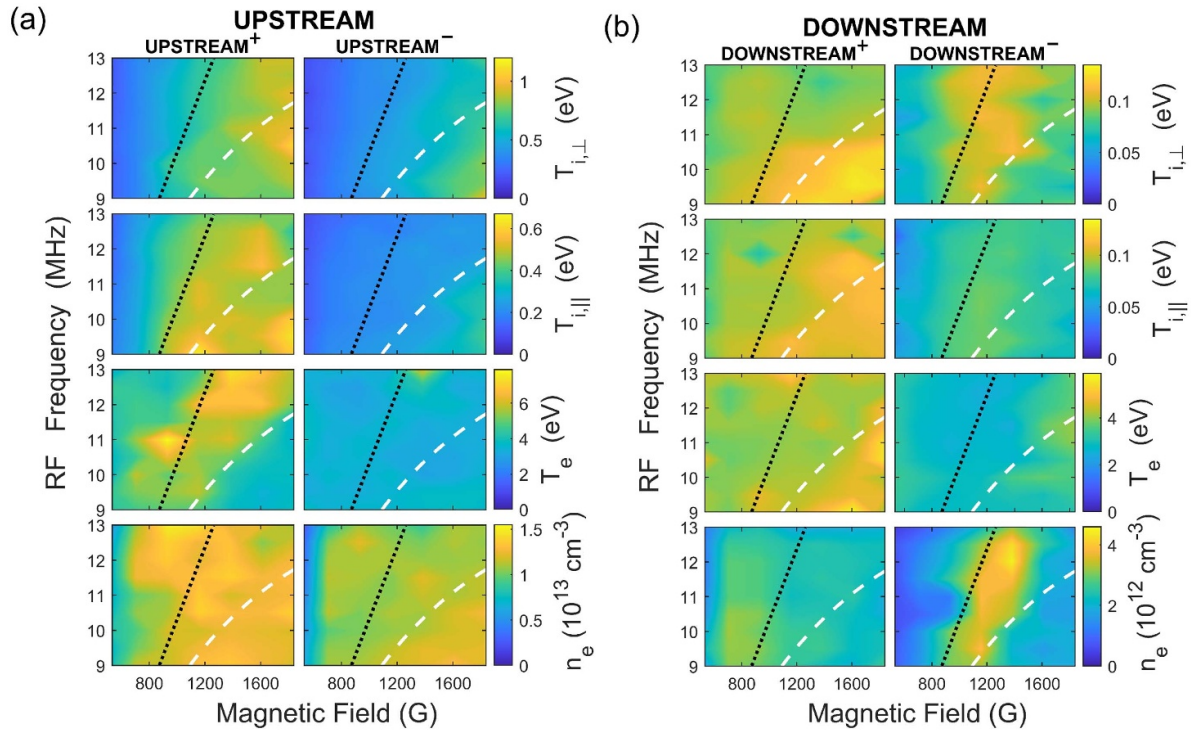


Figure 13. The same upstream and downstream contour plots shown in figure 7 with the on-axis LHF (black dotted line) and the edge LHF (white dashed line) overlaid.

have shown that the density peaks near the antenna or some tens of cm downstream/upstream of the antenna, especially if there is a peak in the background magnetic field strength in that region. Since the magnetic field strength is relatively constant from the antenna region to the measurement location (see figure 3) in these experiments, we have assumed that the density in the antenna region is at least as large as the density at the measurement location. Since the TG mode damps near the edge of the plasma boundary, the density at the edge near the antenna is of particular importance as this is essentially where the LHF resonance would occur. Therefore, the LHF at the antenna would lie somewhere between the black dotted and white dashed lines on figure 13.

For the upstream⁺ case, there is a clear demarcation in ion temperature between antenna frequencies above and below the LHF. There appears to be less correlation between the ion temperatures and the edge LHF. For the upstream⁻ case, it is the edge LHF that bounds the region of enhanced ion temperatures. Somewhat surprising is a clear on-axis, LHF resonance feature in the downstream⁻ ion temperatures (parallel and perpendicular) and the downstream plasma density. The lack of any resonance feature in the downstream⁺ measurements is consistent with RF power dissipation through damping of the helicon wave. The downstream⁻ measurements (as corroborated by magnetic fluctuation measurements presented below) suggest that the helicon wave is completely absent in the downstream⁻ case and that all RF power dissipation occurs through dissipation of the slow wave.

4.5. Helicon wave measurements and theoretical predictions

Regardless of how most of the RF energy is coupled into the plasma, the plasma conditions are ideal for the excitation of the helicon wave in the inner region of the plasma. To confirm that the $m = \pm 1$ helicon waves were launched as predicted to each side of the antenna, and therefore explicitly confirm that the $m = +1$ configuration results in enhanced plasma production, we used a magnetic fluctuation probe to measure the amplitude of the helicon wave as a function of radial location, upstream and downstream of the antenna. The measurements are compared to theoretical models to determine whether the wave is $m = +1$ or $m = -1$ [12]. The expectation was that the magnetic field component amplitudes would match predictions for the $m = +1$ mode for the + cases, and vice versa for the - cases. Downstream⁺ magnetic sense coil measurements are presented in figure 14. The radial wave profiles of the B_z and B_θ components are shown in figure 14(a). The phase shift of each component relative to the antenna phase is shown in figure 14(b). The radial profile of B_θ shows a clear standing wave structure. There is a node (minimum) at $r \approx 1$ cm and the relative phase of B_θ is nearly constant for all radial positions. A traveling wave would exhibit a constantly varying phase with radial location. Note that in these measurements, the apparent large change in phase at $r \approx 2$ cm is a measurement artifact that arises from the 0 to π ambiguity inherent in relative phase measurements. These magnetic field fluctuation component radial profile measurements are very similar to those reported by other groups for excitation of the helicon wave [12, 42]—a single standing wave node in the azimuthal

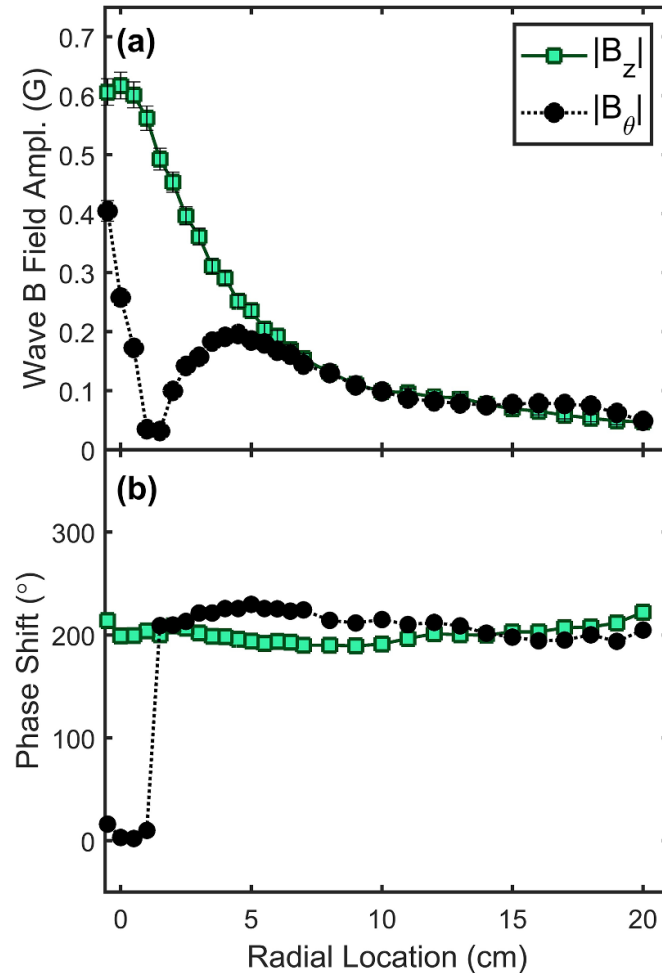


Figure 14. Downstream⁺ configuration. (a) Radial profiles of the downstream magnetic field fluctuation amplitudes for axial and azimuthal components at the antenna frequency. (b) Radial profiles of the relative phase shift of each component relative to the antenna phase. The minimum in B_θ at $r \sim 1$ cm is consistent with a standing wave in the radial direction.

component and an off-axis peak in the axial component of the wave at the antenna frequency.

No measurements are shown for the downstream⁻ case because no detectable wave fields were observed. Three different magnetic fluctuation probes (that successfully measured signals for the downstream⁺ studies) were deployed for the downstream⁻ measurement attempts. Although the antenna helicity and the magnetic field direction are optimal for launching the $m = -1$ helicon wave toward the downstream⁻ region, the $m = -1$ helicon wave was not detected, perhaps due to the wave being absorbed or mode converted before reaching the probe. From the downstream ion and electron measurements, it appears that the slow wave is formed at the plasma edge and is quickly damped (probably due to the rapidly decreasing plasma density as the plasma expands downstream), with enhanced damping at the lower hybrid resonance. Krämer predicted strong damping of the $m = -1$ mode and propagation of the $m = +1$ mode in helicon sources in regions with strong density gradients [43].

The upstream magnetic fluctuation component measurements are less clear. Figure 15 shows the upstream radial profiles for the B_z and B_θ magnetic fluctuations at the antenna

frequency for the upstream⁺ and upstream⁻ magnetic field orientations. The measurements were restricted to $r \geq 2$ cm to prevent the sense coil from melting in the high density plasma core. Numerical predictions for the expected $m = \pm 1$ radial structure at the measured conditions of the experiment were obtained from the HELIC code [44] and compared to the measured helicon wave components. The HELIC code assumes a constant density along the axis of the device, which is not true in PHASMA. HELIC also assumes that the plasma is bounded by a wall with a constant radius along the axis of the device. The experimental system in these experiments is quite different. The antenna region is bounded by a glass wall with a 5.9 cm radius (5.2 cm ID), the upstream region is bounded by a metal wall with a 7.5 cm radius, and the downstream region is bounded with a metal wall with a 20 cm radius. For the the upstream HELIC calculations, the antenna radius was set to $r = 5.9$ cm, the plasma edge was set to $r = 7.4$ cm, and the chamber radius was set to $r = 7.5$ cm to match physical dimensions of the experiment.

In both cases, the measured radial profile of the field components differ significantly from the predictions for the $m = \pm 1$ modes. Looking at the upstream⁺ case, the measured

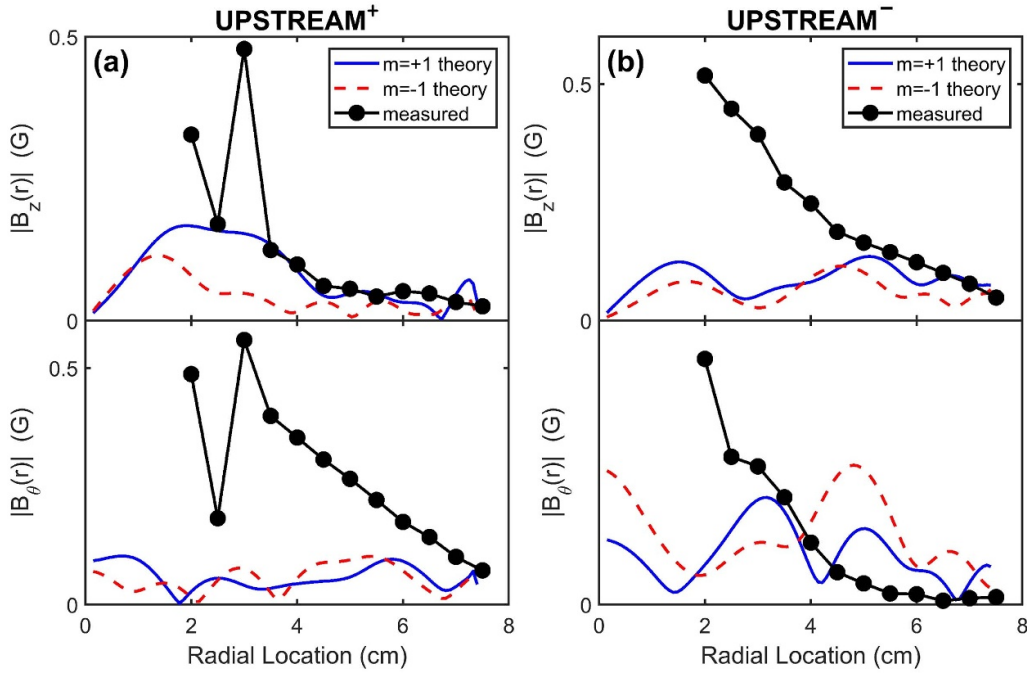


Figure 15. The upstream⁺ case wave B-field B_z and B_θ components (a) and the upstream⁻ case wave B-field components (b) compared to HELIC numerical predictions for $m = \pm 1$ excitation.

component amplitudes increase closer to the plasma axis more quickly than the numerical model predicts. In the upstream⁺ case (see figure 15(a)), the B_z component is somewhat consistent with the $m = +1$ prediction, but there is evidence of radial mode structure in the measurements that does not appear in the model predictions. If the density used in the model calculations is increased (to a few times larger than what is measured), radial mode structure in the predicted B_z component amplitude starts to appear.

While the overall measured radial structure of B_θ is consistent with previous measurements in helicon sources with a $m = +1$ antenna [12], the observed single radial mode structure is inconsistent with the predictions for either the $m = +1$ or $m = -1$ modes. For the upstream⁻ case, the radial mode structure in both components vanishes and the measured component amplitudes increase nearly linearly with decreasing radial location. For both components, the HELIC code fails to predict the measured radial structure. We hypothesize that the measurements are of a superposition of wave modes that are excited by the antenna and arise because of the strong axial and radial inhomogeneities of this helicon source. Direct comparison with the numerical predictions would require measurements using an azimuthal array of magnetic sense coils to separate the amplitudes of the different azimuthal modes. What is clear, however, from all of the upstream magnetic fluctuation measurements is that the wave amplitude at the antenna frequency, the electron temperature, and the ion temperature are largest on axis. Other groups have reported peaked electron temperature profiles that they have attributed to damping of the helicon wave on axis [45].

5. Discussion

The upstream measurements of the perpendicular and parallel ion temperature radial profiles and the dependence on magnetic field magnitude and antenna frequency indicate resonant coupling of RF energy into the plasma around the local LHF. Figure 16 shows the roots of the cold plasma dispersion relation (equation (2)) as a function of the magnetic field strength (bottom x -axis), with the normalized magnetic field strength on the top x -axis (shown here as ω_{LH}/ω for reference to the LHF). The calculations were performed for plasma parameters of $f_{RF} = 10$ MHz, $n = 1 \times 10^{13}$ cm⁻³, $k_{||} = 3.7$ m⁻¹, $T_e = 5$ eV, $T_i = 0.6$ eV, $\nu_i = 3 \times 10^5$ s⁻¹, and $\nu_e = 8 \times 10^6$ s⁻¹. The real solutions to the fast wave (i.e. helicon) and slow wave (i.e. Trivelpiece-Gould) are shown as the dotted blue line and the solid black line, respectively. The dispersion relation for the helicon wave passes through the LHF with no strong resonant features. However, the TG wave has a clear resonance at the LHF and the perpendicular wavenumber becomes large. The perpendicular wavenumber does not go to infinity because of the finite collision frequency used in equation (2). The only way that resonant behavior could appear at the LHF in PHASMA is if there is some coupling of RF power through excitation of the slow wave. Strong damping of the slow wave at the plasma edge is consistent with the perpendicular ion temperature profile measurements.

In summary, the $m = +1$ configuration led to ion and electron temperatures that were up to two times hotter compared to the $m = -1$ configuration. These measurements confirm that for a helicon plasma source with an $m = |1|$ antenna,

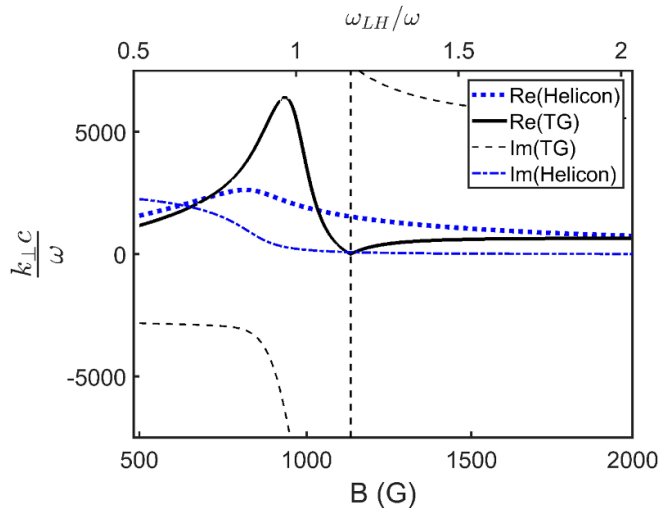


Figure 16. The real and imaginary roots to the cold plasma dispersion relation for $N_{\perp} = k_{\perp}c/\omega$ versus the magnetic field strength with the normalized magnetic field strength shown as ω_{LH}/ω on the top x -axis for reference to the LHF. The parameters for these calculations were $f_{RF} = 10$ MHz, $n = 1 \times 10^{13}$ cm $^{-3}$, $k_{\parallel} = 3.7$ m $^{-1}$, $T_e = 5$ eV, $T_i = 0.6$ eV, $\nu_i = 3 \times 10^5$ s $^{-1}$, and $\nu_e = 8 \times 10^6$ s $^{-1}$.

particle heating and density production depends critically on the orientation of the background magnetic field relative to the antenna helicity. These measurements demonstrate that the level of ion temperature anisotropy, overall ion temperature, and electron temperature are controllable by choice of antenna frequency relative to the LHF and magnetic field direction. The optimal mode of operation (i.e. highest temperatures and density) is when the source frequency is near the LHF and when the system is in the $m = +1$ configuration. Anisotropy was enhanced in the $m = -1$ configuration. Operating in the $m = -1$ configuration is ideal for studies where thermal anisotropy is required. This level of ion thermal anisotropy control is important for fundamental plasma physics studies that seek to excite specific classes of instabilities [46] or studies of plasma etching. Other noteworthy findings include strong evidence of the damping of the TG mode. The resonance features in the downstream $^{-}$ maps (figure 13(b)) combined with the lack of helicon wave structures in the magnetic fluctuation measurements for the downstream $^{-}$ case, and the lack of resonance features appearing in the downstream $^{+}$ case, suggest that the TG resonance is likely responsible for heating the ions in the downstream $^{-}$ case. Moreover, the edge perpendicular ion heating observed in the upstream $^{+}$ case provides further confirmation of the damping of the TG mode near the edge of the plasma.

Data availability statement

The data that support the findings of this study are available upon reasonable request from the authors.

Acknowledgments

This work was supported by NSF Award PHY 1902111.

ORCID iDs

K J Stevenson  <https://orcid.org/0000-0001-7574-8193>

E E Scime  <https://orcid.org/0000-0003-4128-492X>

References

- [1] Balkey M, Boivin R, Kline J and Scime E 2001 *Plasma Sources Sci. Technol.* **10** 284–94
- [2] Kline J L, Scime E E, Boivin R F, Keesee A M, Sun X and Mikhailenko V S 2002 *Phys. Rev. Lett.* **88** 195002
- [3] Chen G, Arefiev A V, Bengtson R D, Breizman B N, Lee C A and Raja L L 2006 *Phys. Plasmas* **13** 123507
- [4] Aguirre E M, Scime E E, Thompson D S and Good T N 2017 *Phys. Plasmas* **24** 123510
- [5] Bennet A, Charles C and Boswell R 2018 *J. Phys. D: Appl. Phys.* **51** 375204
- [6] Cho S 1996 *Phys. Plasmas* **3** 4268
- [7] Wong K L and Ono M 1981 *Phys. Rev. Lett.* **47** 842–5
- [8] Scime E E, Carr J J, Galante M, Magee R M and Hardin R 2013 *Phys. Plasmas* **20** 032103
- [9] Aguirre E M, Bodin R, Yin N, Good T N and Scime E E 2020 *Phys. Plasmas* **27** 123501
- [10] Caneses J F, Blackwell B D and Piotrowicz P 2017 *Phys. Plasmas* **24** 113513
- [11] Chabert P and Braithwaite N 2011 *8.2.4 Antenna Coupling* (Cambridge University Press)
- [12] Light M and Chen F F 1995 *Phys. Plasmas* **2** 1084
- [13] Blackwell D D and Chen F F 1997 *Plasma Sources Sci. Technol.* **6** 569
- [14] Suzuki K S K, Nakamura K N K and Sugai H S H 1996 *Jpn. J. Appl. Phys.* **35** 4044
- [15] Miljak D G and Chen F F 1998 *Plasma Sources Sci. Technol.* **7** 61
- [16] Granetzny M, Schmitz O and Zepp M 2023 *Phys. Plasmas* **30** 120701
- [17] Hesse M and Cassak P A 2020 *J. Geophys. Res.: Space Phys.* **125** e2018JA025935
- [18] Shi P, Srivastav P, Barbhuiya M H, Cassak P A, Scime E E and Swisdak M 2022 *Phys. Rev. Lett.* **128** 025002
- [19] Beatty C B, Steinberger T E, Aguirre E M, Beatty R A, Klein K G, McLaughlin J W, Neal L and Scime E E 2020 *Phys. Plasmas* **27** 122101
- [20] Zhang X, Aguirre E, Thompson D S, McKee J, Henriquez M and Scime E E 2018 *Phys. Plasmas* **25** 23503
- [21] Thompson D S, Khaziev R, Fortney-Henriquez M, Keniley S, Scime E E and Curreli D 2020 *Phys. Plasmas* **27** 73511
- [22] Boivin R F and Scime E E 2003 *Rev. Sci. Instrum.* **74** 4352–60
- [23] Keesee A M, Scime E E and Boivin R F 2004 *Rev. Sci. Instrum.* **75** 4091–3
- [24] Galante M E, Magee R M and Scime E E 2014 *Phys. Plasmas* **21** 055704
- [25] Thompson D S, Steinberger T E, Keesee A M and Scime E E 2018 *Plasma Sources Sci. Technol.* **27** 065007
- [26] Shi P, Srivastav P, Beatty C, Nirwan R S and Scime E E 2021 *Rev. Sci. Instrum.* **92** 033102
- [27] Shi P and Scime E 2023 *Rev. Sci. Instrum.* **94** 023501
- [28] Biloiu I A and Scime E E 2010 *Phys. Plasmas* **17** 113509

- [29] Chu F, Hood R and Skiff F 2019 *Phys. Plasmas* **26** 042111
- [30] Lee Y K and Chung C W 2011 *J. Appl. Phys.* **109** 013306
- [31] Sun X, Biloiu C, Hardin R and Scime E E 2004 *Plasma Sources Sci. Technol.* **13** 359
- [32] Severn G D, Edrich D A and McWilliams R 1998 *Rev. Sci. Instrum.* **69** 10–15
- [33] Boivin R 2003 *EPAPS-E-PHPAEN-10-003306* PL-050 West Virginia University
- [34] Demidov V, Ratynskaia S V and Rypdal K 2002 *Rev. Sci. Instrum.* **73** 3409–39
- [35] Godyak V A and Demidov V I 2011 *J. Phys. D: Appl. Phys.* **44** 233001
- [36] Gilbert T J, Stevenson K J, Paul M C, Steinberger T E and Scime E E 2021 *AIP Adv.* **11** 055314
- [37] Shamrai K P and Taranov V B 1996 *Plasma Sources Sci. Technol.* **5** 474
- [38] Zhao Y, Bai J, Cao Y, Wu S, Ahedo E, Merino M and Tian B 2022 *Chin. Phys. B* **31** 075203
- [39] Chen F F, Sudit I D and Light M 1996 *Plasma Sources Sci. Technol.* **5** 173
- [40] Chang L, Hole M J, Caneses J F, Chen G, Blackwell B D and Corr C S 2012 *Phys. Plasmas* **19** 083511
- [41] Blackwell B D, Caneses J F, Samuel C M, Wach J, Howard J and Corr C 2012 *Plasma Sources Sci. Technol.* **21** 055033
- [42] Shoji T, Sakawa Y, Nakazawa S, Kadota K and Sato T 1993 *Plasma Sources Sci. Technol.* **2** 5
- [43] Krämer M 1999 *Phys. Plasmas* **6** 1052–8
- [44] Arnush D 2000 *Phys. Plasmas* **7** 3042
- [45] Niemi K, von der Gathen V S and Döbele H F 2001 *J. Phys. D: Appl. Phys.* **34** 2330–5
- [46] Scime E E, Keiter P A, Balkey M M, Boivin R F, Kline J L, Blackburn M and Gary S P 2000 *Phys. Plasmas* **7** 2157–65